Depth-Dependent Redox Behavior of $LiNi_{0.6}Mn_{0.2}Co_{0.2}O_2$

Chixia Tian,[1] Dennis Nordlund,[2] Huolin L. Xin,[3] Yahong Xu,[2,4] Yijin Liu,[2] Dimosthenis Sokaras,[2] Feng Lin,[5] and Marca M. Doeff[1*]

1. Energy Storage & Distributed Resources Division, Lawrence Berkeley National Laboratory, Berkeley, California 94720, USA.
2. Stanford Synchrotron Radiation Lightsource, SLAC National Accelerator Laboratory, Menlo Park, California 94025, USA.
3. Center for Functional Nanomaterials, Brookhaven National Laboratory, Upton, New York 11973, USA.
4. College of Mechanical Engineering, Donghua University, Shanghai 200051, China
5. Department of Chemistry, Virginia Tech, Blacksburg, Virginia 24061, USA.

* corresponding author: e-mail: mmdoeff@lbl.gov

Abstract

Nickel-rich layered materials are emerging as cathodes of choice for next-generation high energy density lithium ion batteries intended for electric vehicles. This is because of their higher practical capacities compared to compositions with lower Ni content, as well as the potential for lower raw materials cost. The higher practical capacity of these materials comes at the expense of shorter cycle life, however, due to undesirable structure and chemical transformations, especially at particle surfaces. To understand these changes more fully, the charge compensation mechanism and bulk and surface structural changes of $LiNi_{0.6}Mn_{0.2}Co_{0.2}O_2$ were probed using synchrotron techniques and electron energy loss spectroscopy in this study. In the bulk, both the crystal and electronic structure changes are reversible upon cycling to high voltages, whereas particle surfaces undergo significant reduction and structural reconstruction. While Ni is the major contributor to charge compensation, Co and O (through transition metal-oxygen hybridization) are also redox active. An important finding from depth-dependent transition metal L-edge and O K-edge X-ray spectroscopy is that oxygen redox activity exhibits depth-dependent characteristics. This likely drives the structural and chemical transformations observed at particle surfaces in Ni-rich materials.

The need for lithium-ion batteries with higher energy density and lower cost than currently available, particularly for transport applications, has led to intensified interest in Ni-rich NMC ($LiNi_xMn_yCo_zO_2$; $x+y+z\approx1$, where $x>y$) cathode materials.[1–5] These materials deliver higher practical capacities in a typically used voltage range than NMCs with lower Ni content (e.g., $LiNi_{1/3}Mn_{1/3}Co_{1/3}O_2$ or NMC-333), and most formulations contain less of the expensive Co component, reducing raw material costs. The increase in practical capacity roughly scales with the Ni content, but comes at the expense of cycle life and thermal stability at high states-of-charge (SOC).[6]

To circumvent these problems, several different strategies have been utilized to improve cycling, particularly to higher potentials. These include partial substitution with Ti[7–9] or Zr,[10] engineering the micro- or nano-structure to reduce surface Ni content using metal segregation,[11] surface pillared structures,[12] and concentration gradients,[13] coating particle surfaces,[14] and development of electrolyte additives.[15,16] While all of these approaches have resulted in improvements, further understanding of the factors that lead to capacity fading is clearly needed in order to meet the stringent performance requirements of traction applications.

The formation of a resistive cathode/electrolyte interphase (CEI), such as an electrolyte decomposition layer, has been observed during cycling of $LiNi_{0.4}Mn_{0.4}Co_{0.2}O_2$ (NMC-442) electrodes, particularly when high voltage limits were used.[17] This leads to cell impedance rise and an effective loss of capacity. In addition, rock salt or mixed rock salt/spinel phases on particle surfaces have been detected under various cycling or storage conditions for NMC-442,[18] $LiNi_{0.5}Mn_{0.3}Co_{0.2}O_2$ (NMC-532),[19] and $LiNi_{0.8}Mn_{0.1}Co_{0.1}O_2$ (NMC-811).[20] In the study of NMC-532, it was found that surface reconstruction to a

65 rock salt phase dominates when high voltage (4.8V) cutoffs are used due to oxygen loss
66 under the highly oxidizing conditions, while spinel forms under milder cycling
67 conditions. In contrast, predominantly rock salt phases, rather than spinel, were observed
68 on NMC-442 particle surfaces even when cells were cycled to conservative limits, or
69 during storage without electrochemical operation, although reconstruction was more
70 severe during high voltage cycling. In the case of NMC-811, no obvious bulk crystal
71 structure changes were observed after extensive cycling (200 cycles) and parasitic
72 reactions between the highly delithiated cathode surface and electrolyte were suggested
73 as the major contributor to capacity fading.[15,20] However, for the parent compound
74 $LiNiO_2$, it has been found that degradation of the bulk crystal structure contributes to
75 capacity fading.[21] Two phase conversions (H1 to H2, and H2 to H3) occur during
76 delithiation/lithiation of $LiNiO_2$, with H3 formation occurring at high SOC during
77 cycling. In contrast, this phase is rarely encountered during cycling of NMCs, as it occurs
78 outside the normal operating voltage range.[22] The degradation of cycling performance for
79 $LiNiO_2$ is associated with the loss of the H3 phase during long term cycling. These
80 observations suggest that a systematic investigation of surface and bulk phenomena
81 involved in cycling Ni-rich NMCs is needed to determine the driving factors for capacity
82 fading.

83 In this work, we present a comprehensive investigation of the crystal and
84 electronic structure changes of $LiNi_{0.6}Mn_{0.2}Co_{0.2}O_2$ (NMC-622), both at the surface and
85 in the bulk. Towards this end, we employed a combination of synchrotron *in-operando*
86 X-ray diffraction (XRD), soft X-ray absorption spectroscopy (soft XAS) with different
87 detection modes to probe different depth, annular dark-field scanning transmission

electron microscopy (ADF-STEM) and electron energy loss spectroscopy (EELS). By probing the electronic structure of both the transition metal ions and lattice oxygen during the first cycle and long term cycling, we were able to correlate the surface reconstruction to highly reactive surface oxygen. These results suggest that surface treatments may be the best approach for improving cycle life of Ni-rich NMCs by slowing down the kinetics of interfacial reactions.

Experimental Section

Synthesis of $LiNi_{0.6}Mn_{0.2}Co_{0.2}O_2$

NMC-622 pristine powder was synthesized by ultrasonic spray pyrolysis followed by thermal annealing. The general procedure has been reported in previous publications.[11,23,24] Different parameters, including precursor solution concentration, injection rate, gas carrier flow rate and spray pyrolysis temperature, were studied to optimize the synthesis conditions. For the material used in this study, the following conditions were used. A 2M aqueous solution of $LiNO_3$ (Sigma Aldrich), $Ni(NO_3)_2 \cdot 6H_2O$ (Sigma Aldrich), $Co(NO_3)_2 \cdot 6H_2O$ (Sigma Aldrich) and $Mn(NO_3)_2$ (45−50 wt% solution in dilute nitric acid, Sigma Aldrich) with a molar ratio of 1.2:0.6:0.2:0.2 was prepared and transferred into a syringe pump. The solution was injected at a flow rate of 0.25 ml/min and sprayed into micro-sized droplets using a 120 kHz wide spray ultrasonic atomizer, which generates droplets with an average size of 12.5 μm. The droplets were then carried into a preheated horizontal quartz tube (700 ^{o}C) by air with a flow rate of 10 liters per minute (LPM). The as-synthesized powder was then collected and further annealed in air box furnace for 4 hrs at 480 ^{o}C and 4 hrs at 850 ^{o}C, using a ramping rate of 2 ^{o}C/min.

Electrode preparation and electrochemical studies

A composite electrode slurry was prepared containing active material, polyvinylidene fluoride (PVdF) (Kureha Chemical Ind. Co. Limited) in N-methyl-2-pyrrolidinone (6%, wt%), and acetylene carbon black (Denka, 50% compressed), with solid matter ratios of 84:8:8 and cast onto carbon-coated aluminum current collectors (Coveris). The electrodes were then dried in a vacuum oven overnight at 120^{o}C and cut to size. Typical active material areal loadings were 2.0–2.5 mg cm^{-2}. 2032 coin cells using these cathodes, Li metal as the negative electrode, Celgard 2400 as the separator, and 1 M $LiPF_6$ solution in 1:1 v/v ethylene carbonate/diethyl carbonate (EC-DEC, Novolyte Technologies) as the electrolytic solution were assembled in an argon-filled glove box. Cells were allowed to rest for 12 hrs before testing with a VMP3 potentiostat/galvanostat (BioLogic) system. Galvanostatic cycling was performed at C/10, where 1C is defined as the theoretical capacity of NMC-622, i.e., 276 mAh g^{-1}, discharged or charged in one hour. For post characterization, the electrodes were collected from disassembled coin cells, rinsed with dimethyl carbonate and dried in an argon-filled glove box.

Materials characterization

To determine phase purity, powder XRD patterns were collected using a Bruker D2 Phaser diffractometer with Cu Kα radiation. Pristine powder was dissolved in concentrated nitric acid and analyzed with an inductively coupled plasma optical emission spectrometer (ICP-OES, Perkin-Elmer Optima5400) to determine the chemical composition. Scanning electron microscopy (SEM) was performed on a JEOL JSM-7000F with a Thermo Scientific energy dispersive X-ray spectroscopy (EDS) detector. The ADF-STEM imaging was performed on a 200 keV cold-field-emission probe-

corrected instrument equipped with an Enfina EELS at Brookhaven National Laboratory. For soft XAS experiments, samples were mounted on an aluminum sample holder with double-sided carbon tape in an argon-filled glove box, transferred in a double-contained jar to a glove bag purged with argon connected to the XAS load-lock chamber. Measurements were conducted on the bending magnet beamline 8-2 at Stanford Synchrotron Radiation Lightsource (SSRL) using a ring current of 500 mA and a 1100 lines*mm^{-1} spherical grating monochromator. The monochromator was operated with 40μm entrance and exit slits, providing~2.0×10^{10} ph s^{-1} at 0.4 eV resolution in a 0.1 x 0.1 mm^2 beam spot. Data were acquired under ultrahigh vacuum (10^{-9} Torr) in a single load at room temperature using Auger electron yield (AEY, measured by a cylindrical mirror analyzer at constant kinetic energy), total electron yield (TEY, measured by sample drain current) and Fluorescence Yield (FY, measured with an IRD AXUV-100 silicon diode). All spectra were normalized by the current from a gold-evaporated fine grid positioned upstream of the main chamber. For transition metal L-edges, a linear fit background was removed and then the maximum intensities are normalized to unity. This normalization method has negligible effect for the transition metal L-edge data interpretation since the peak position (e.g., Co L-edge)/peak shape (e.g., Mn L-edge) or the relative peak intensity ratio (e.g., Ni L_3 high to L_3 low peak intensity ratio) were used to quantify the oxidation states. However, oxygen K-edge data was normalized using a different method, where a linear background fit to the pre-edge region (520 eV to 525 eV) was subtracted from the spectra and the post-edge (565 eV to 580 eV) was normalized to unity. For samples that have lithium carbonate layers on the surface, a correction was applied; details are discussed in supporting information. *Operando*

synchrotron X-ray diffraction studies were performed at beamline 11−3 at SSRL. The coin cell components (bottom case, spacer and top cap) were pierced with 2mm holes. Kapton tape was used to cover the holes on the bottom cases and top caps. The cells were then assembled the same way as other 2032 coin cells. Aluminum tabs were attached to either sides of the coin cell and sealed in a polyester pouch. See reference[25] for further details. The cell was cycled at a rate of 28 mA g^{-1} (~0.6 mA/cm^2). Transmission XRD ring patterns were detected using a MAR image plate and were collected every minute. Selected patterns (every 20 mins) were plotted in this work. LaB_6 patterns were collected as reference data for calibration, and exposure time was only a half second for the samples to avoid any saturation. For ease of comparison, all data was converted to same pattern as the Bruker Cu Kα (λ=1.54 Å) format. A blank cell containing all other components except the active cathode material was also assembled and measured, as shown in Figure S1. Therefore, peaks attributable to the Kapton tape and the packing pouch bag could be identified, and a background could be subtracted.

Results and Discussion

Characterization of pristine NMC-622 materials

An SEM image of NMC-622 pristine powders is shown in Figure 1a. The secondary particles consist of agglomerated primary particles ranging in size from 200 nm to 800 nm (Figure 1a inset) and have a spherical shape about 5μm to 13μm across in diameter (Figure 1a). The resulting NMC-622 materials are phase pure and all reflections in the XRD pattern (Figure 1b) can be indexed to the $R\bar{3}m$ space group with the layered rhombohedral structure of α-$NaFeO_2$. The high-resolution STEM image in Figure 1c reveals the nearly ideal layered structure where almost no transition metals occupy the Li

channels (lithium ions are not visible in the STEM imaging). STEM-EELS analysis was performed for the particle shown in Figure 1d (red dashed arrow shows the direction of EELS scanning) and show that the oxidation states of three transition metals (i.e., Mn, Co and Ni) and oxygen remain almost unchanged from the surface to the bulk (Figure 1e).

We also used ensemble-averaged synchrotron soft XAS to characterize the pristine material. The beam size of 1 x 1 mm^2 characterizes millions of sub-micron sized primary particles simultaneously, complementing the STEM-EELS experiment, in which only one or a few particles can be probed. In addition to delivering ensemble-averaged information, the three different detection modes, namely AEY, TEY and FY, of synchrotron based soft XAS have the capability of probing different depths (AEY, 1-2 nm; TEY, ~5 nm; FY, ~50-100 nm). Soft XAS transition metal (TM) L-edge experiments directly probe the dipole allowed 2p-3d transition of transition metals, which provides unique fingerprint of their valence states and the detailed multiplet structure is also sensitive to spin and symmetry.[26] The spectra of transition metals are spin-orbit split into an L_3-edge ($2p_{3/2}$) at lower energy and an L_2-edge ($2p_{1/2}$) at higher energy. XAS L-edge spectra of Mn and Co (Figure 2a and Figure 2b) in AEY, TEY and FY modes show identical shapes and peak intensities, which suggest that the oxidation states of Mn and Co are homogeneous from the surface to the bulk. The valence states are further determined to be Mn^{4+} and Co^{3+} as expected. For the Ni L-edge spectra, about 17 eV separates the Ni L_3 and the Ni L_2 peaks. As shown in Figure 2c, the Ni L_3 multiplet structure has the most spectral weight in two locations (peak A in the lower energy region and peak B in the higher energy region) in the L_3 edge absorption band (for details of the electronic structure origin based on spin and symmetry of the Ni center, see reference 26.

The relative intensity ratio for peak B/peak A can be utilized as an indicator for changes of oxidation states.[18,21] The ratio increases as Ni is oxidized. Comparing the relative intensities of these two peaks in the different modes shows that the surface Ni (AEY and TEY in Figure 2c) is slightly reduced in comparison to the bulk. A similar phenomenon was also detected for $LiNiO_2$,[21,27] which suggests that there is instability of surface Ni in nickel-rich materials before electrochemical cycling and even without any interaction with the electrolytic solution. However, the surface reduction of Ni for the NMC-622 material is minimal, and the average oxidation state is still much higher than Ni^{2+} (orange dashed line in Figure 2c represents $LiNi_{1/3}Mn_{1/3}Co_{1/3}O_2$, where all Ni cations are in the Ni^{2+} oxidation state). The results from soft XAS are consistent with the EELS analysis, collectively demonstrating a homogeneous distribution of electronic structures for all the transition metal cations in the pristine material with minimal reduction of Ni at particle surfaces.

The O K-edge data is shown in Figure 2d. The O K-edge includes a higher energy region (>535 eV) associated with O 1s transitions to hybridized TM4sp-O2p states and a lower energy region (<535 eV) originating from O 1s transition to TM3d-O2p hybridized states.[28] The lower energy region is of most interest here. Four peaks or shoulders (labeled 1, 2, 3, and 4 in Figures 2d and 2e) can be assigned by comparison to standard samples. Red open circles depict the FY data and black open circles the TEY data for the pristine NMC-622 in Figure 2e. Peak 1 (~528.5 eV) corresponds to the Ni^{3+} 3d-O 2p hybridized state, as is found in $LiNiO_2$ (orange curve in Figure 2e). Peak 2, which is relatively broad and centered around 530 eV, can be attributed to Mn^{4+} 3d-O 2p hybridization, although Co^{3+} 3d-O 2p and Ni^{3+} 3d-O 2p may also contribute, as evidenced

by a comparison with $LiCoO_2$ (brown curve) and $LiNiO_2$ (orange curve). Peak 3 (~532eV) mainly arises from the contribution of Mn^{4+} 3d-O 2p (pink curve for MnO_2) although Ni^{2+} 3d-O 2p (blue curve for NiO) may also contribute. In this region, there is some overlap of TM-O signals.[29–31] However, while some Ni^{2+} (as well as Ni^{3+}) is expected to be present in the pristine material, it is significant that this peak is stronger in the TEY mode than in FY mode. This is consistent with the observation in the Ni L-edge data that Ni on the surface is marginally more reduced than it is in the bulk. A sharp peak around 534 eV (peak 4 in Figure2e) matches the green curve for pure Li_2CO_3. Li_2CO_3 is frequently observed as a stable by-product on particle surfaces of nickel-rich lithium-host materials.[6,21,27] This peak is only observed in AEY and TEY mode (Figure 2d) and not in FY mode (Figure 2d), showing that Li_2CO_3 is present on surfaces only a few nm deep.

Changes in bulk and surface electronic structures during the initial cycle

NMC electrodes are commonly cycled to 4.3V in lithium half-cells, with practical capacities rising as the Ni content is increased, although the theoretical limit of ~280 mAh/g is not attained.[2,6,32] Raising the charge voltage limit to 4.7V vs. Li^+/Li results in increased utilization,[9] but lower capacity retention upon cycling due to rising cell impedance.[17,18] Figure S2 shows capacity retention data for half cells containing NMC-622 cycled to various voltage limits. Because of the presence of lithium carbonate on particle surfaces, the initial cycle discharge capacity is lower than on subsequent cycles when cells are charged to 4.7V. After the second cycle to 4.7V, a maximum discharge capacity of 202 mAh/g was reached, while the cell charged to 4.3V reached its maximum capacity after 6 cycles.

Bulk crystal structure changes leading to microstrain,[33] cracking,[34] and disconnection[35] have been implicated in cycling losses of layered oxide materials. Synchrotron based *in operando* XRD offers the opportunity to capture subtle structure changes while performing electrochemistry simultaneously. Data for a Li/NMC-622 cell were collected for the initial charge and discharge processes at a rate of about C/10 between 2.5 V to 4.7 V. Representative patterns are plotted as a function of cell voltage in Figure 3a. The charge-discharge profile for in situ XRD is also shown here, with the corresponding lithium content calculated from the coulometry. Note that, because of differences in the *in situ* cell configuration compared to the *ex situ* cells, the discharge capacity is somewhat lower than that found for regular cells. The NMC-622 cathode material showed behavior intermediate between that of NMC-333[22] and $LiNiO_2$[36] or $LiNi_{0.8}Co_{0.15}Al_{0.05}O_2$ (NCA) in terms of the phase behavior. The H1+H2 two-phase region occurs over a narrower voltage window in NMC-333 and the H3 phase only appears at potentials above 5V vs. Li/Li^+. In the case of NMC-622, two hexagonal phases (H1 and H2) co-exist between 3.83-3.9V, with the H3 phase appearing only near 5V (Figure S3). Because cells are rarely cycled to such high potentials, the capacity fading associated with the large volume change of the H2 to H3 transition in the Li_xNiO_2 system[21] can be completely avoided.

The excellent reversibility of the NMC-622 cathode when cycled between 2.5 and 4.7V in a lithium half-cell is evident from the patterns in Figure 3a. The lattice parameter and cell volume changes are shown in Figure 3b and c. As lithium ions are removed from the structure, the *c* lattice parameter initially expands while the *a* lattice parameter decreases. Above 4.2V, a dramatic contraction of the *c*-axis with slight expansions along

271 the *a*-axis and *b*-axis are observed. However, these processes are completely reversible,
272 and the overall volume change upon delithiation to 4.7V (approximately 90% delithiated
273 in the *in situ* cell) is only about 4%. The results indicate that the bulk crystal structure
274 remains quite stable and reversible during redox processes, consistent with that reported
275 in the literature.[15]

276 Soft XAS was used to monitor the electronic structure changes at both the surface
277 and the bulk, as a function of SOC of the NMC-622 cathode. For these experiments,
278 electrodes were collected from partially and fully charged or discharged half-cells and
279 characterized *ex situ*. Data from both TEY and FY modes of the L_3 edges of the three
280 transition metals are plotted in Figure 4. As shown in Figure 4a, no change is observed
281 for Mn from the surface sensitive TEY spectra and bulk sensitive FY spectra, indicating
282 that Mn^{4+} remains electrochemically inactive in NMC-622 during cycling, as expected.
283 However, there is some variation observed between the Mn FY and TEY modes for the
284 50% and 100% charged samples. We hypothesize the small distortion is most likely due
285 to self-absorption and saturation effects, based on the analysis in reference 37. It has been
286 reported that inverse-partial-FY (IPFY) XAS would suppress this distortion. However,
287 we believe the small distortion is not related to the redox activity of Mn as more
288 significant changes for both the line shape and intensity would be expected.[38] In contrast,
289 Co L_3-edge XAS spectra shift to higher energy in charged and partially charged
290 electrodes and back to lower energies in the discharged electrodes. The shifting indicates
291 that Co is partly oxidized during charge and reduced during the discharge (Figure 4c).
292 The behavior of Co is similar at the surface and in the bulk. The L_3 peak position is
293 consistent with trivalent Co in the pristine electrode, and shifts from 780.9 eV to 781.3

294 eV at the top of charge for a total difference of 0.4 eV. In comparison, Co^{3+} to Co^{4+}
295 changes in model compounds not only involves an larger absolute energy shift but also
296 show another peak for Co^{4+} at lower energy in the L_3 region.[39,40] This indicates that Co in
297 NMC-622 is not fully charged to Co^{4+} and only partially contributes to the charge
298 compensation during lithium deintercalation and intercalation processes under these
299 conditions.

300 The most dramatic changes occur with Ni, however, both on the surface and in the
301 bulk (Figure 4a). As discussed earlier, the relative intensity ratios of the higher to lower
302 energy L_3 peaks track the oxidation state changes of nickel. These ratios are plotted as a
303 function of SOCs in Figure 4d, showing that there are significant changes in the redox
304 states of Ni upon charging and discharging, both in TEY and FY modes. Therefore, it can
305 be concluded that redox processes involving Ni are the major contributors to charge
306 compensation in NMC-622 during cycling. However, the surface nickel (TEY) is
307 consistently more reduced than the bulk nickel (FY) at different SOCs, indicating that the
308 surface activity is different from that of the bulk. Similar surface phenomena have been
309 reported for other systems such as $LiNi_{0.8}Co_{0.2}O_2$[41–43] and $LiNiO_2$[27].

310 Figures 5a and b shows the O K-edge data for electrodes at different SOCs. For
311 the pristine electrode (black curve) and the 50% charged electrode (red curve), there is a
312 peak at 534 eV in the TEY spectra, which can be assigned to the oxygen in Li_2CO_3. This
313 peak was not observed for the same electrodes in the FY mode, indicating that the Li_2CO_3
314 layer is surface-bound and relatively thin. In the electrode charged to 4.7V, however, the
315 O K-edge of Li_2CO_3 disappeared completely due to the electrochemical decomposition of
316 Li_2CO_3 at high potentials.

317 The intensity of the TM3d-O2p states in the O K-edge, originate from the
318 O1s→O2p dipole transition into unoccupied hybridized states which has gained O2p
319 character through the covalent interaction, where both the degree of covalency and the
320 total number of unoccupied d-states determine the total oscillator strength.[28]
321 Phenomenologically, the integrated intensity in this region (region #1 in Figures 5a and
322 5b) will thus represent the redox activity of the oxygen, since the effective number of
323 holes in the oxygen (through the TM-O interaction) is proportional to this area.[44] We note
324 that there is an increase in the number of unoccupied states in the TM3d-O2p hybridized
325 orbitals as a function of lithium deintercalation. This can be attributed to the greater
326 number of d-holes and the sharing of these holes with the oxygen ligands, as well as the
327 associated increase in covalency that further shifts hole distribution onto the ligands. In
328 order to extract semi-quantitatively the redox activity of the oxygen, the integrated
329 intensity in the lower energy region (<534 eV) is plotted for the samples at various SOCs
330 (Figures 5c and d). Note that in order to compare the strength of the pre-edge relative to
331 the ionization potential, the spectra need to be consistently normalized at higher energies,
332 and compounds other than lattice oxygen (such as the carbonate at the surface) have been
333 subtracted and then the spectrum re-normalized (see pristine and 50% charged in Figures
334 5c and 5d, where the orange error bars reflect the errors in the subtraction procedure;
335 details are discussed in the supporting information and shown in Figures S4 and S5). In
336 addition, for the integrated sums in Figure 5d, we first performed a self-absorption
337 correction to the FY spectra (violet error bars) in order to allow comparison of oscillator
338 strengths at various intensities without non-linear artifacts (Figure S6). It is noted that

such a rigorous data processing for oxygen K-edge quantification has sometimes been neglected in the literature.

Comparing the data in TEY and FY modes (Figure 6), we found that the integrated intensity of TM3d-O2p hybridization peak was much higher in the FY mode in the pristine and fully discharged electrodes, indicating that the bulk in the NMC-622 particles has more TM3d-O2p unoccupied states under these conditions. This is consistent with the Ni L-edge soft XAS data, where Ni has a higher oxidation state in the bulk compared to the surface. Secondly, we observed that the change of the integrated intensity was more dramatic in the TEY mode, which strongly suggests that the surface region of the NMC-622 material underwent more dynamic changes of hole states in the TM3d-O2p hybridization. The relative integrated intensity change is only ~18% in the bulk (FY) but is ~33% (TEY) on the surface going from the pristine state to that in the electrode charged to 4.7 V. Interference from the Li_2CO_3 signal required special normalization procedures for the data obtained from the pristine and partially charged electrodes (see experimental and supporting information sections for details). More reliable data can be obtained from the 100% charged, 50% discharged and 100% discharged electrodes, where Li_2CO_3 is absent from the surfaces. Even for these electrodes, there is a discrepancy observed between the surface and the bulk with 23% and 12% changes, respectively, going from the fully charged electrode to the one discharged to 2.5 V. The observation is consistent with the fact that the surfaces of NMC materials usually undergoes more dramatic structural changes after extended cycles (as discussed below).

There has been much debate about the possible role that oxygen plays in layered transition metal oxide redox processes during electrochemical cycling, particularly when high voltage cutoffs are used with Li-rich materials.[45–47] It has also been reported that oxygen anions are involved in charge compensation through reversible charge redistribution between transition metal and oxygen in spinel[48] and layered oxides (e.g., NMC-333[49]). However, for the NMC-333 material, only the TEY mode was used to investigate the oxygen K-edge in that study, which only provided information about surface oxygen. In studies reported by Yoon et al., both surface (TEY) and bulk (FY) oxygen activities were investigated for $LiNi_{0.5}Mn_{0.5}O_2$,[50] NMC-333,[51] $LiCoO_2$,[52] NCA,[30] and $LiNiO_2$[27] materials. The conclusions in these studies were that oxygen anions participated more significantly in the charge compensation (through core-hole distribution) when Co cations were present, and the surface and bulk oxygen activities became more distinct in high Ni content layered materials than in NMCs with lower Ni content.

To investigate the effect of cycling on these phenomena, STEM-EELS and soft XAS to investigate the structural transformation of NMC-622 materials after an extended number of cycles between 2.5-4.7 V was carried out. First, a series of EELS spectra (Figure 7) were collected as a function of distance from the surface to the bulk of an NMC-622 particle extracted from an electrode cycled 50 times and stopped at 2.5V. In all three transition metals, there were consistent shifts of L_3 peaks towards higher energies as the EELS scanning moved from the surface into the bulk. Conversely, O K-edge peaks shifted to lower energies from the surface to the bulk because of increased TM3d-O2p unoccupied states in the bulk. In addition, the O pre-edge features associated with TM3d-

O2p hybridization became stronger along the same scanning direction (Figure 7b). These collectively show that there was a significant buildup of reduced transition metals at the surfaces of the intensively cycled NMC particles. The STEM image (Figure 7d) shows that in the surface region, the lithium channels were occupied by transition metals, consistent with a transition from a layered structure to a rock-salt structure, although the transition was not as complete as seen for NMC-442 in previous studies.[17,18,53] Figure 7e clearly shows that the bulk retains the original layered structure with open Li channels. Ensemble-averaged soft XAS was also used to complement the observations made by STEM-EELS. As shown in Figure 7c, Mn, Co and Ni all underwent substantial reduction upon intensive cycling. Moreover, all three transition metals were more reduced on the surface (TEY) than in the bulk (FY). The oxygen K-edge XAS has lower integrated peak intensity after 50 cycles than after 1 cycle. This phenomenon is more pronounced on the surface (green curve in Figure 7c), which is consistent with the observed surface reconstruction, and suggests that the process may continue to occur even after numerous cycles.

Clearly, steps to decrease the reactivity of surface oxygen are necessary to improve the electrochemical performance of Ni-rich NMCs, particularly if the goal is to cycle to higher potentials to access higher practical capacities. To this end, certain strategies, such as partial Ti substitution[7–9,54]and coatings,[55] as well as the use of electrolyte additives[56] should prove useful.

Conclusions

In pristine NMC-622, Ni has an average valence state higher than 2+, while Mn is tetravalent and cobalt is trivalent. A thin layer of lithium carbonate is present on particle

surfaces, which decomposes during charge to high voltages. *In operando* XRD on NMC-622 electrodes undergoing charge to 4.7V and discharge to 2.5V show that the bulk structural changes are highly reversible, with an overall volume change of 4% when charged to 4.7V. Soft XAS studies indicate that both nickel and cobalt undergo redox during delithiation and lithiation processes, but that Ni in the bulk behaves differently from that on particle surfaces. A rigorous and detailed analysis of the oxygen K-edge spectra indicates the surface oxygen has higher reactivity than the bulk. These two observations taken together indicate that there is more charge compensation on oxygen on particle surfaces than in the bulk. This is a driving force for surface reconstruction and the formation of surface films (CEI) that increase cell impedance and lead to capacity fading. Surface reconstruction on NMC-622 is observed after one cycle and becomes more apparent after long cycling. Our study also highlights the importance of combining high spatial resolution STEM-EELS and ensemble-averaged XAS, with improved statistics, to eliminate the discrepant conclusion of chemical environment.

Acknowledgments

This work was supported by the Assistant Secretary for Energy Efficiency and Renewable Energy, Office of Vehicle Technologies of the U.S. Department of Energy under Contract No. DE-AC02-05CH11231. This research used resources of the Center for Functional Nanomaterials, which is a U.S. DOE Office of Science Facility, at Brookhaven National Laboratory under Contract No. DE-SC0012704. The synchrotron X-ray portions of this research were carried out at the Stanford Synchrotron Radiation Lightsource, a Directorate of SLAC National Accelerator Laboratory and an Office of

Science User Facility operated for the U.S. Department of Energy Office of Science by Stanford University. Use of the Stanford Synchrotron Radiation Lightsource, SLAC National Accelerator Laboratory, is supported by the U.S. Department of Energy, Office of Science, Office of Basic Energy Sciences under Contract No. DE-AC02-76SF00515. F.L. gratefully acknowledges Virginia Tech Department of Chemistry startup funds. C.T. would like to acknowledge Dr. Yanbao Fu from Lawrence Berkeley National Lab and Dr. Douglas Van Campen from SLAC for their help with the experiments.

Additional Information

Supplementary information is available on-line.

References

1. J. Xu, F. Lin, M. M. Doeff, and W. Tong, *J. Mater. Chem. A*, **5**, 874–901 (2017)

2. W. Liu, P. Oh, X. Liu, M.-J. Lee, W. Cho, S. Chae, Y. Kim and J. Cho, *Angew. Chem. Int. Ed. Engl.*, **54**, 4440–57 (2015)

3. B. Xu, D. Qian, Z. Wang, and Y. S. Meng, *Mater. Sci. Eng. R Reports*, **73**, 51–65 (2012).

4. N. Nitta, F. Wu, J. T. Lee, and G. Yushin, *Mater. Today*, **18**, 252–264 (2015)

5. A. Manthiram, B. Song, and W. Li, *Energy Storage Mater.*, **6**, 125–139 (2017)

6. H.-J. Noh, S. Youn, C. S. Yoon, and Y.-K. Sun, *J. Power Sources*, **233**, 121–130 (2013).

7. S. Wolff-Goodrich, F. Lin, I. M. Markus, D. Nordlund, H. L. Xin, M. Asta and M. M. Doeff, *Phys. Chem. Chem. Phys.*, **17**, 21778–21781 (2015)

8. K. C. Kam and M. M. Doeff, *J. Mater. Chem.*, **21**, 9991 (2011)

9. K. C. Kam, A. Mehta, J. T. Heron, and M. M. Doeff, *J. Electrochem. Soc.*, **159**, A1383–A1392 (2012)

10. F. Schipper, M. Dixit, D. Kovacheva, M. Talianker, O. Haik, J. Grinblat, E. M. Erickson, C. Ghanty, D. T. Major, B. Markovsky and D. Aurbach, *J. Mater. Chem. A*, **4**, 16073–16084 (2016)

11. F. Lin, D. Nordlund, Y. Li, M. K. Quan, L. Cheng, T.-C. Weng, Y. Liu, H. L. Xin and M. M. Doeff, *Nat. Energy*, **1**, 15004 (2016)

12. Y. Cho, P. Oh, and J. Cho, *Nano Lett.*, **13**, 1145–1152 (2013)

13. Y.-K. Sun, S.-T. Myung, B.-C. Park, J. Prakash, I. Belharouak and K. Amine, *Nat. Mater.*, **8**, 320–324 (2009)

14. I. H. Son, J. H. Park, S. Kwon, J. Mun, and J. W. Choi, *Chem. Mater.*, **27**, 7370–7379 (2015)

15. J. Li, L. E. Downie, L. Ma, W. Qiu, and J. R. Dahn, *J. Electrochem. Soc.*, **162**, 1401–1408 (2015).

16. X. Zhao, Q.-C. Zhuang, C. Wu, K. Wu, J.-M. Xu, M.-Y. Zhang and X.-L. Sun, *J. Electrochem. Soc.*, **162**, A2770–A2779 (2015)

17. F. Lin, D. Nordlund, I. M. Markus, T.-C. Weng, H. L. Xin and M. M. Doeff, *Energy Environ. Sci.*, **7**, 3077 (2014)

18. F. Lin, I. M. Markus, D. Nordlund, T.-C. Weng, M. D. Asta, H. L. Xin and M. M. Doeff, *Nat. Commun.*, **5**, 3529 (2014)

19. S.-K. Jung, H. Gwon, J. Hong, K.-Y. Park, D.-H. Seo, H. Kim, J. Hyun, W. Yang and K. Kang, *Adv. Energy Mater.*, **4**, 1300787 (2014)

20. J. Li, H. Liu, J. Xia, A. R. Cameron, M. Nie, G. A. Botton and J. R. Dahn, *J. Electrochem. Soc.*, **164**, A655–A665 (2017)

21. J. Xu, E. Hu, D. Nordlund, A. Mehta, S. N. Ehrlich, X.-Q. Yang and W. Tong, *ACS Appl. Mater. Interfaces*, **8**, 31677–31683 (2016)

22. W.-S. Yoon, K. Y. Chung, J. McBreen, and X.-Q. Yang, *Electrochem. commun.*, **8**, 1257–1262 (2006)

23. J. Liu, T. E. Conry, X. Song, L. Yang, M. M. Doeff and T. J. Richardson, *J. Mater. Chem.*, **21**, 9984–9987 (2011)

24. J. Liu, T. E. Conry, X. Song, M. M. Doeff, and T. J. Richardson, *Energy Environ. Sci.*, **4**, 885 (2011)

25. M. M. Doeff, G. Chen, J. Cabana, T. J. Richardson, A. Mehta, M. Shirpour, H.

501 Duncan, C. Kim, K. C. Kam and T. Conry, *J. Vis. Exp.*, e50594 (2013)

502 26. F. M. F. de Groot, J. C. Fuggle, B. T. Thole, and G. A. Sawatzky, *Phys. Rev. B*, **42**,

503 5459–5468 (1990)

504 27. W. S. Yoon, K. Y. Chung, J. McBreen, D. A. Fischer, and X.-Q. Yang, *J. Power*

505 *Sources*, **163** (2006)

506 28. F. M. F. De Groot, M. Gnom, J. C. Fuggle, J. Ghijsen, G. A. Sawatzky, H. Petersen,

507 B. Elektronenspeicherring-Gesellschaft, S. M and H. Sy, *Phys. Rev. B*, **40**, 15–1989

508 29. Y. Uchimoto, H. Sawada, and T. Yao, *J. Power Sources*, **97**–**98**, 326–327 (2001)

509 30. W.-S. Yoon, K. Y. Chung, J. McBreen, D. A. Fischer, and X.-Q. Yang, *J. Power*

510 *Sources*, **174**, 1015–1020 (2007)

511 31. W. S. Yoon, M. Balasubramanian, K. Y. Chung, X. Q. Yang, J. McBreen, C. P. Grey

512 and D. A. Fischer, *J. Am. Chem. Soc.*, **127**, 17479–17487 (2005).

513 32. C. S. Yoon, M. H. Choi, B.-B. Lim, E.-J. Lee, and Y.-K. Sun, *J. Electrochem. Soc.*,

514 **162**, A2483–A2489 (2015)

515 33. E.-J. Lee, Z. Chen, H.-J. Noh, S. C. Nam, S. Kang, D. H. Kim, K. Amine and Y.-K.

516 Sun, *Nano Lett.*, **14**, 4873–4880 (2014)

517 34. N. Kızıltaş-Yavuz, M. Herklotz, A. M. Hashem, H. M. Abuzeid, B. Schwarz, H.

518 Ehrenberg, A. Mauger and C. M. Julien, *Electrochim. Acta*, **113**, 313–321 (2013).

519 35. R. Hausbrand, G. Cherkashinin, H. Ehrenberg, M. Gröting, K. Albe, C. Hess and W.

520 Jaegermann, *Mater. Sci. Eng. B*, **192**, 3–25 (2015).

521 36. X. . Yang, X. Sun, and J. McBreen, *Electrochem. commun.*, **1**, 227–232 (1999).

522 37. D. Asakura, E. Hosono, Y. Nanba, H. Zhou, J. Okabayashi, C. Ban, P.-A. Glans, J.

523 Guo, T. Mizokawa, G. Chen, A. J. Achkar, D. G. Hawthron, T. Z. Regier and H. Wadati,

524 *AIP Adv.*, **6**, 35105 (2016).
525 38. R. Qiao, Y. Wang, P. Olalde-Velasco, H. Li, Y.-S. Hu and W. Yang, *J. Power*
526 *Sources*, **273**, 1120–1126 (2015).
527 39. R. H. Potze, G. A. Sawatzky, and M. Abbate, *Phys. Rev. B*, **51**, 11501–11506 (1995)
528 40. H.-J. Lin, Y. Y. Chin, Z. Hu, G. J. Shu, F. C. Chou, H. Ohta, K. Yoshimura, S.
529 Hébert, A. Maignan, A. Tanaka, L. H. Tjeng and C. T. Chen, *Phys. Rev. B*, **81**, 115138
530 (2010)
531 41. D. P. Abraham, J. Liu, C. H. Chen, Y. E. Hyung, M. Stoll, N. Elsen, S. Maclaren, R.
532 Twesten, R. Haasch, E. Sammann, I. Petrov, K. Amine and G. Henriksen, *J. Power*
533 *Sources*, **119**–**121**, 511–516 (2003)
534 42. D. P. Abraham, R. D. Twesten, M. Balasubramanian, I. Petrov, J. Mcbreen and K.
535 Amine, *Electrochem. commun.*, **4**, 620–625 (2002)
536 43. D. P. Abraham, R. D. Twesten, M. Balasubramanian, J. Kropf, D. Fischer, J.
537 McBreen, I. Petrov and K. Amine, *J. Electrochem. Soc.*, **150**, A1450 (2003)
538 44. J. Suntivich, W. T. Hong, Y.-L. Lee, J. M. Rondinelli, W. Yang, J. B. Goodenough,
539 B. Dabrowski, J. W. Freeland and Y. Shao-Horn, *J. Phys. Chem. C*, **118**, 1856–1863
540 (2014)
541 45. K. Luo, M. R. Roberts, R. Hao, N. Guerrini, D. M. Pickup, Y.-S. Liu, K. Edström, J.
542 Guo, A. V. Chadwick, L. C. Duda and P. G. Bruce, *Nat. Chem.*, **8**, 1–17 (2016)
543 46. R. Yuge, A. Toda, S. Kuroshima, H. Sato, T. Miyazaki, N. Tamura, M. Tabuchi and
544 K. Nakahara, *Electrochim. Acta*, **189**, 166–174 (2016)
545 47. M. Oishi, K. Yamanaka, I. Watanabe, K. Shimoda, T. Matsunaga, H. Arai, Y. Ukyo,
546 Y. Uchimoto, Z. Ogumi and T. Ohta, *J. Mater. Chem. A*, **4**, 9293–9302 (2016)

547 48. J. Zhou, D. Hong, J. Wang, Y. Hu, X. Xie and H. Fang, *Phys. Chem. Chem. Phys.*,
548 **16**, 13838–13842 (2014)
549 49. M. G. Kim, H. J. Shin, J.-H. Kim, S.-H. Park, and Y.-K. Sun, *J. Electrochem. Soc.*,
550 **152**, A1320 (2005)
551 50. W.-S. Yoon, M. Balasubramanian, X.-Q. Yang, Z. Fu, D. A. Fischer and J. McBreen,
552 *J. Electrochem. Soc.*, **151**, A246 (2004)
553 51. W.-S. Yoon, Y. Paik, X.-Q. Yang, M. Balasubramanian, J. McBreen and C. P. Grey,
554 *Electrochem. Solid-State Lett.*, **5**, A263 (2002)
555 52. W. S. Yoon, K. B. Kim, M. G. Kim, M. K. Lee, H. J. Shin, J. M. Lee, J. S. Lee and C.
556 H. Yo, *J. Phys. Chem. B*, **106**, 2526–2532 (2002).
557 53. F. Lin, D. Nordlund, T. Pan, I. M. Markus, T.-C. Weng, H. L. Xin, M. M. Doeff and
558 M. M. Doe, *J. Mater. Chem. A*, **2**, 19833–19840 (2014)
559 54. I. M. Markus, F. Lin, K. C. Kam, M. Asta and M. M. Doeff, *J. Phys. Chem. Lett.*, **5**,
560 3649–3655 (2014)
561 55. X. Fang, F. Lin, D. Nordlund, M. Mecklenburg, M. Ge, J. Rong, A. Zhang, C. Shen,
562 Y. Liu, Y. Cao, M. M. Doeff and C. Zhou, *Adv. Funct. Mater.*, **27**, 1602873 (2017)
563 56. S. R. Li, N. N. Sinha, C. H. Chen, K. Xu, and J. R. Dahn, *J. Electrochem. Soc.*, **160**,
564 A2014–A2020 (2013)
565
566
567
568
569

570

571

572

573

574

575

576

577

578

579 **Figure Captions**

580 **Figure 1.** (a) SEM images of secondary particles and (inset) primary particles of NMC-
581 622 prepared by spray pyrolysis. (b) XRD pattern with Rietveld refinement. (c) High-
582 resolution Z-contrast ADF-STEM image of NMC-622 primary particle. (d) EELS survey
583 image and (e) EELS spectra integrated from surface to bulk (red arrow direction) of the
584 area in the green box in Figure 1 (d).

585

586 **Figure 2.** Soft XAS spectra of pristine NMC-622 (a) Mn L-edge, (b) Co L-edge and (c)
587 Ni L-edge (orange dashed line is for NMC-333 material used as a Ni^{2+} reference) and (d)
588 O K-edge using AEY (black), TEY (red) and FY (blue) modes. (e) Soft XAS O K-edge
589 spectra of different standard samples (blue for NiO, green for Li_2CO_3, pink for MnO_2,
590 brown for $LiCoO_2$ and orange for $LiNiO_2$) and pristine NMC-622 (black circled curve for
591 TEY/surface and red circled curve for FY/bulk). Numbers 1, 2, 3 and 4 labeled in d and e
592 are identical.

Figure 3. a) *In situ* synchrotron XRD patterns of the first charge and discharge of an NMC-622 cathode between 2.5 V and 4.7 V at a C/10 (1C=270mAh/g) rate. Reflections are indexed. The blue asterisks represent the aluminum current collector and the green # signs are associated with polymer components (i.e., separator, kapton tape and polyester pouch material). Cell potentials are given at the right of the figure. (b) Lattice constants evolution (black and red circles represent lattice constant c while pink and green circles represent lattice constant a for H1 and H2 phase during charge; Bright and dark blue triangles are lattice constant c and a during discharge) and (c) unit cell volume change (black squares for H1 phase and red spheres for H2 phase during charge; blue triangles for volume change during discharge) of NMC-622 as a function of time during the first cycle.

Figure 4. (a) Mn, Co and Ni L_3-edge soft XAS spectra of electrodes at various SOCs in TEY (solid lines) and FY (dashed lines) modes and (b) the corresponding voltage profile of the initial cycle. (c) Absolute peak energy shifting of Co L_3-edge and (d) relative intensity ratio between Ni L_3 high energy peak (peak B) to low energy peak (peak A) (Ni $L_{3\ high}/L_{3\ low}$) at different SOCs in TEY (open squares) and FY (solid spheres) modes. Different colors represent various SOCs in a-d: black-pristine electrode; red-50% charged; blue-100% charged (4.7 V); pink-50% discharged; green-100% discharged (2.5 V).

Figure 5. O-K edge soft XAS spectra of electrodes at various SOCs in (a) TEY and (b) FY modes. Region #1 (green shaded area) includes pre-edge features associated with TM3d-O2p hybridization states and region #2 (pink shaded area) a fingerprint of surface Li_2CO_3. Integrated peak areas (region 1 only) of TEY and FY data are shown in (c) and (d), respectively. Different colors represent various SOCs: black-pristine electrode; red-50% charged; blue-100% charged (4.7 V); pink-50% discharged; green-100% discharged (2.5 V). Orange error bars in (c) and (d) are based on a correction by removing surface Li_2CO_3 layer contribution to the post-edge normalization; violet error bars are associated with "self-absorption effect" correction under FY mode. The dashed gray lines are added for visual enhancement.

Figure 6. Comparative integrated relative peak areas of region #1 in a) TEY and b) FY modes through peak fitting from the data shown in Figure 5 for electrodes at various states-of-charge. Orange error bars are based on a correction by removing surface Li_2CO_3 layer contribution to the post-edge normalization; violet error bars are associated with "self-absorption effect" correction under FY mode. The dashed gray lines are added for visual enhancement.

Figure 7. a) EELS spectra of O, Mn, Co and Ni integrated from the surface to the bulk of primary particle that was cycled to 4.7 V 50 times and stopped at 2.5V. The distance from the surface to the bulk is 12 nm. The red dashed line corresponds to the peak energy on the surface, while the green dashed line corresponds to the peak energy in the bulk. (b) Integrated peak intensity of O pre-edge in the lower energy region as a function of EELS

638 scanning depth. The red arrow shows an increasing integrated intensity (increasing
639 number of unoccupied states) from the surface to the bulk. (c) Soft XAS spectra of O K-
640 edge, Mn, Co and Ni L_3-edge of electrodes collected after 1 cycle and 50 cycles and
641 stopped in the discharged state. Black curve- 1cycle TEY mode; red curve-1 cycle FY
642 mode; green curve- 50 cycles TEY mode; blue curve-50 cycles FY mode. Representative
643 STEM images of NMC-622 primary particles after 50 cycles (d) on the surface and (e) in
644 the bulk (the white and green arrows indicate the Li channels).
645

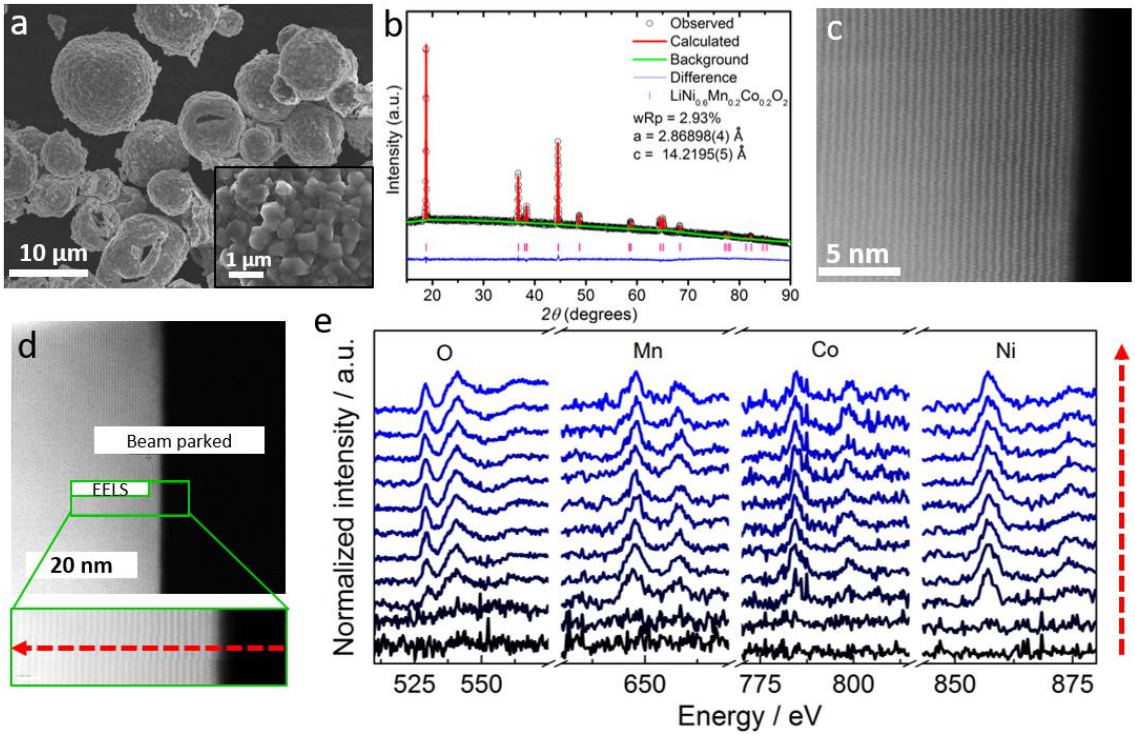
a
10 µm
1 µm
b
Observed
Calculated
Background
Difference
LiNi0.6Mn0.2Co0.2O2
wRp = 2.93%
a = 2.86898(4) Å
c = 14.2195(5) Å
Intensity (a.u.)
2θ (degrees)
c
5 nm
d
Beam parked
EELS
20 nm
e
O
Mn
Co
Ni
Normalized intensity / a.u.
Energy / eV

Figure 1

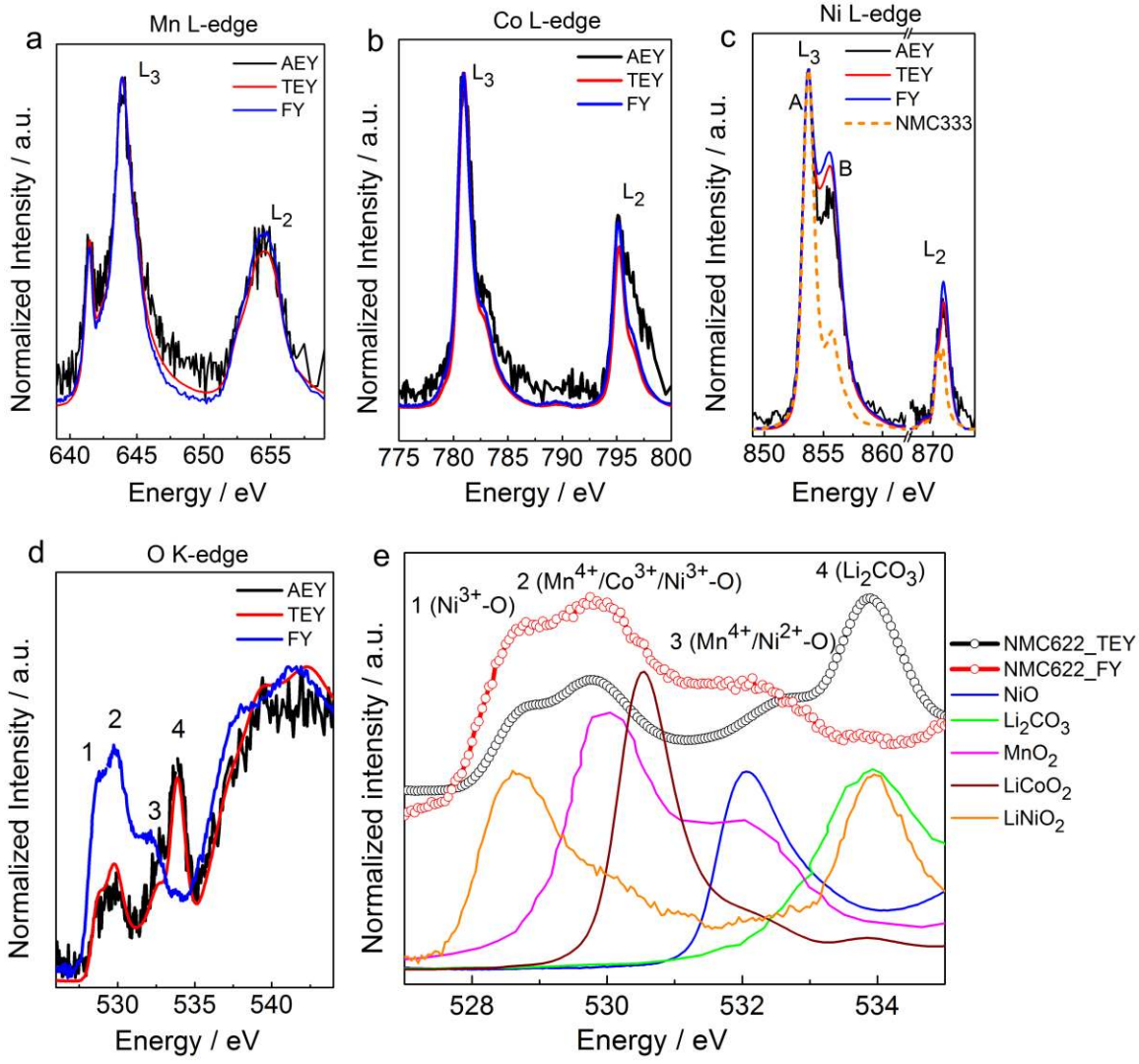
a
Mn L-edge
AEY
TEY
FY
L3
L2
Normalized Intensity / a.u.
640 645 650 655
Energy / eV
b
Co L-edge
AEY
TEY
FY
L3
L2
Normalized Intensity / a.u.
775 780 785 790 795 800
Energy / eV
c
Ni L-edge
AEY
TEY
FY
NMC333
L3
A
B
L2
Normalized Intensity / a.u.
850 855 860 870
Energy / eV
d
O K-edge
AEY
TEY
FY
1
2
3
4
Normalized Intensity / a.u.
530 535 540
Energy / eV
e
1 (Ni3+-O)
2 (Mn4+/Co3+/Ni3+-O)
3 (Mn4+/Ni2+-O)
4 (Li2CO3)
NMC622_TEY
NMC622_FY
NiO
Li2CO3
MnO2
LiCoO2
LiNiO2
Normalized intensity / a.u.
528 530 532 534
Energy / eV

Figure 2

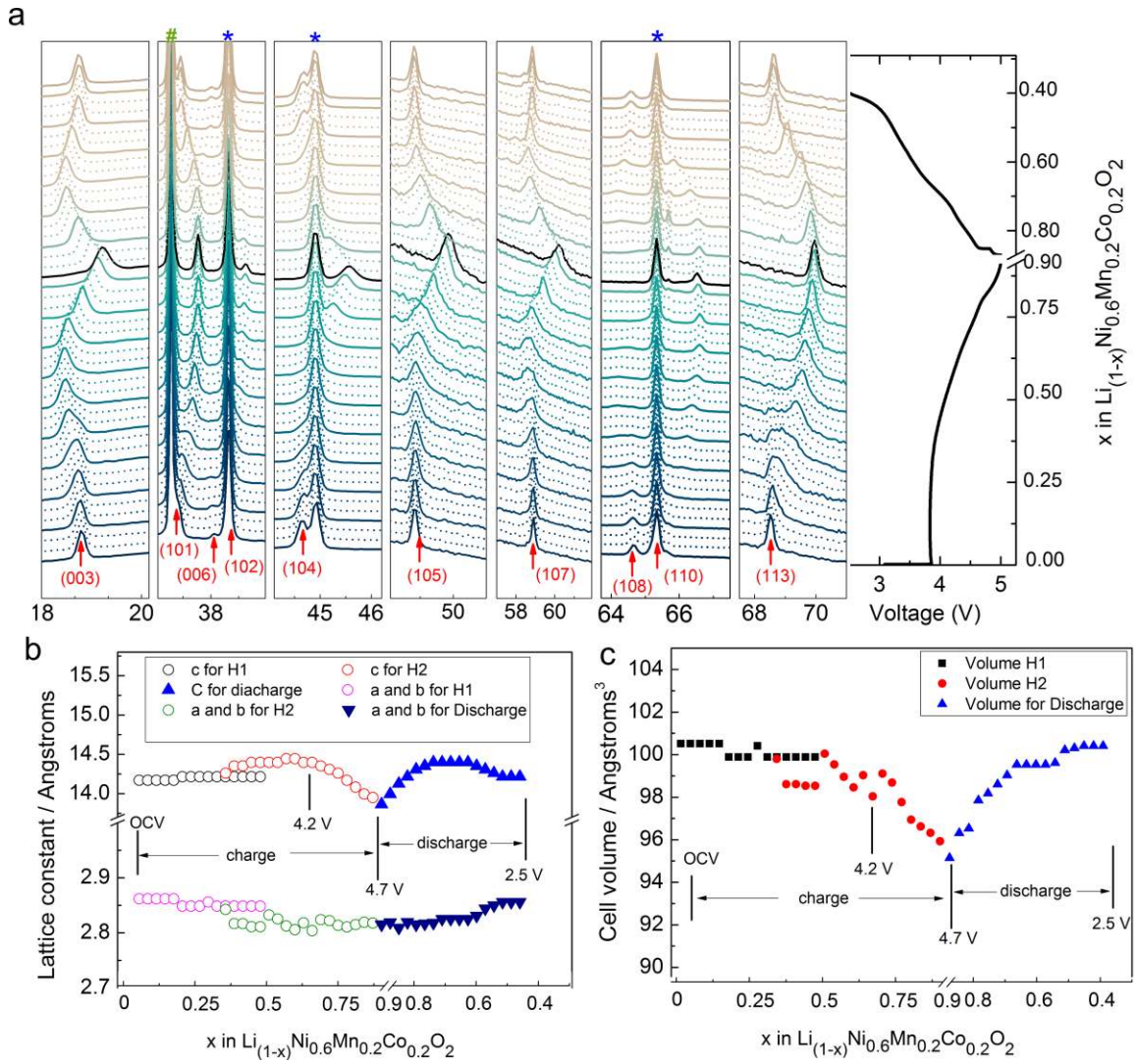
a
#
*
*
*
(003)
(101)
(006)
(102)
(104)
(105)
(107)
(108)
(110)
(113)
18
20
38
45
46
50
58
60
64
66
68
70
3
4
5
Voltage (V)
0.40
0.60
0.80
0.90
0.75
0.50
0.25
0.00
x in Li(1-x)Ni0.6Mn0.2Co0.2O2
b
c for H1
C for diacharge
a and b for H2
c for H2
a and b for H1
a and b for Discharge
Lattice constant / Angstroms
OCV
charge
4.2 V
4.7 V
discharge
2.5 V
x in Li(1-x)Ni0.6Mn0.2Co0.2O2
c
Volume H1
Volume H2
Volume for Discharge
Cell volume / Angstroms3
OCV
charge
4.2 V
4.7 V
discharge
2.5 V
x in Li(1-x)Ni0.6Mn0.2Co0.2O2

Figure 3

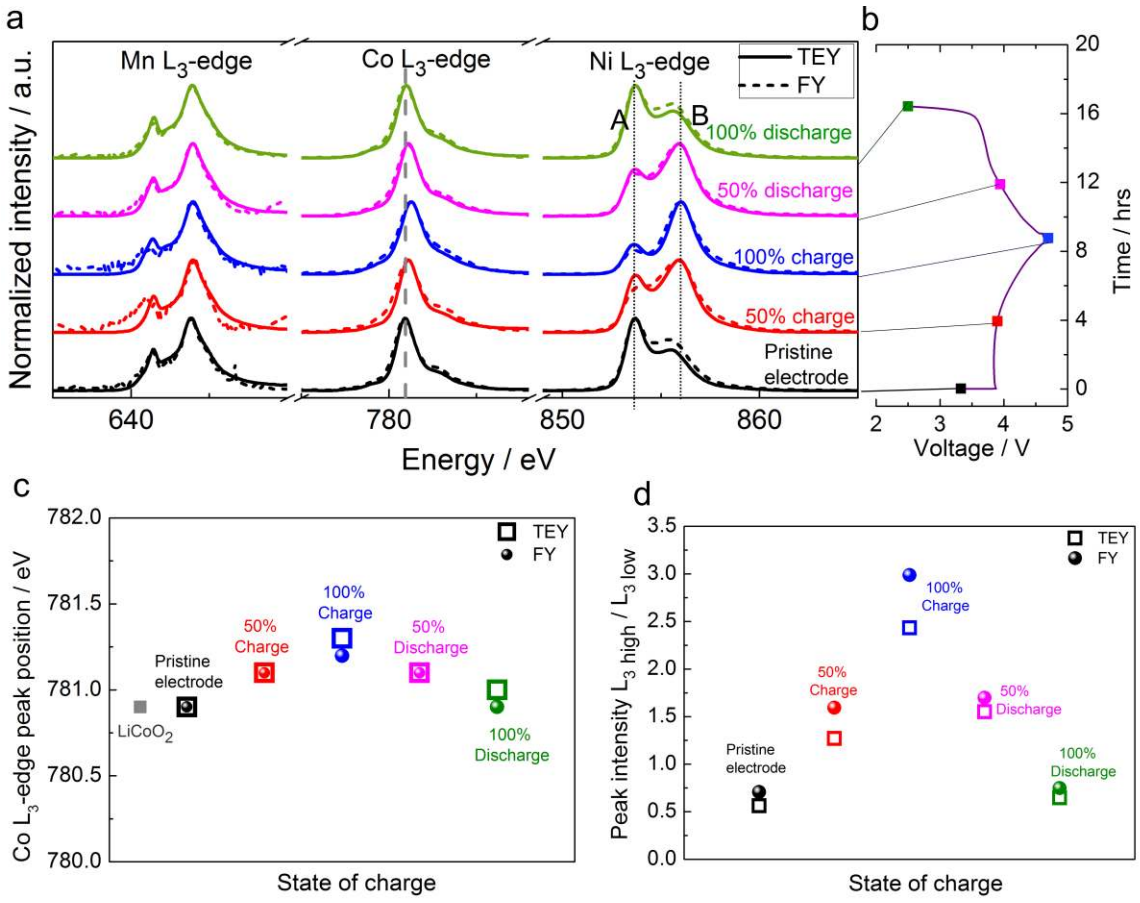
a
Mn L3-edge
Co L3-edge
Ni L3-edge
TEY
FY
A
B
100% discharge
50% discharge
100% charge
50% charge
Pristine electrode
Normalized intensity / a.u.
640
780
850
860
Energy / eV
b
Time / hrs
Voltage / V
c
Co L3-edge peak position / eV
Pristine electrode
LiCoO2
50% Charge
100% Charge
50% Discharge
100% Discharge
State of charge
d
Peak intensity L3 high / L3 low
State of charge

Figure 4

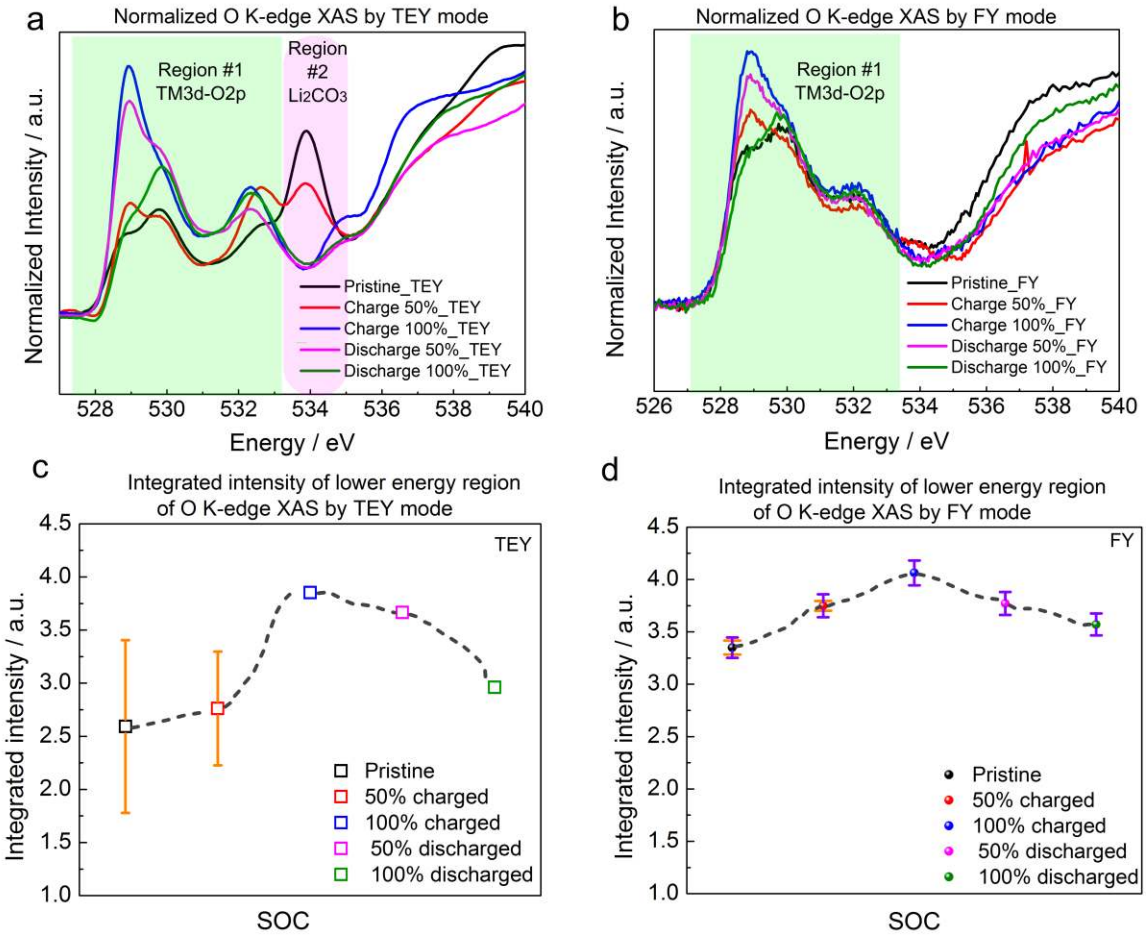
a
Normalized O K-edge XAS by TEY mode
Region #1
TM3d-O2p
Region
#2
Li2CO3
Normalized Intensity / a.u.
Energy / eV
Pristine_TEY
Charge 50%_TEY
Charge 100%_TEY
Discharge 50%_TEY
Discharge 100%_TEY
b
Normalized O K-edge XAS by FY mode
Region #1
TM3d-O2p
Normalized Intensity / a.u.
Energy / eV
Pristine_FY
Charge 50%_FY
Charge 100%_FY
Discharge 50%_FY
Discharge 100%_FY
c
Integrated intensity of lower energy region
of O K-edge XAS by TEY mode
TEY
Integrated intensity / a.u.
SOC
Pristine
50% charged
100% charged
50% discharged
100% discharged
d
Integrated intensity of lower energy region
of O K-edge XAS by FY mode
FY
Integrated intensity / a.u.
SOC
Pristine
50% charged
100% charged
50% discharged
100% discharged

Figure 5

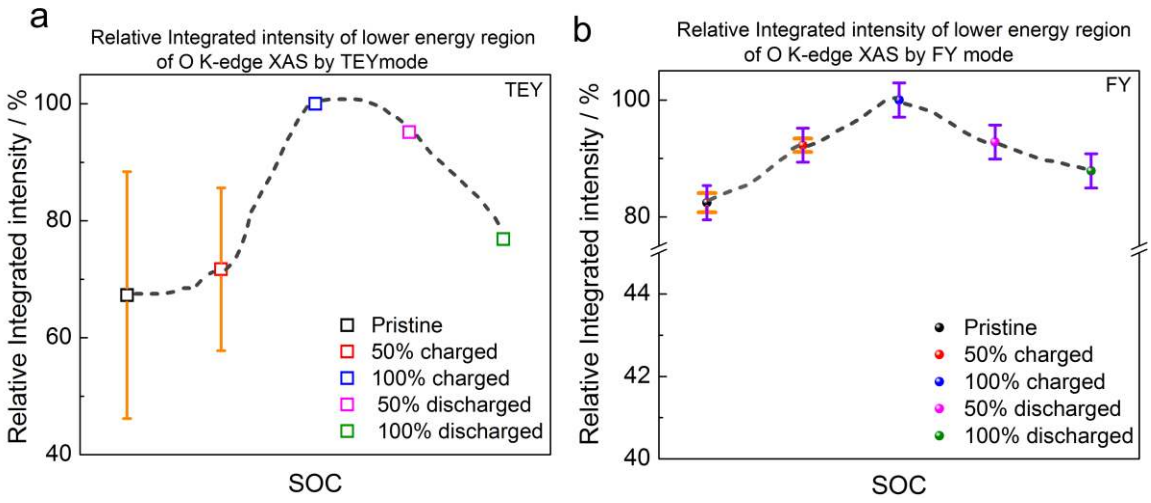
a
Relative Integrated intensity of lower energy region
of O K-edge XAS by TEYmode
TEY
Relative Integrated intensity / %
100
80
60
40
SOC
Pristine
50% charged
100% charged
50% discharged
100% discharged
b
Relative Integrated intensity of lower energy region
of O K-edge XAS by FY mode
FY
Relative Integrated intensity / %
100
80
44
42
40
SOC
Pristine
50% charged
100% charged
50% discharged
100% discharged

Figure 6

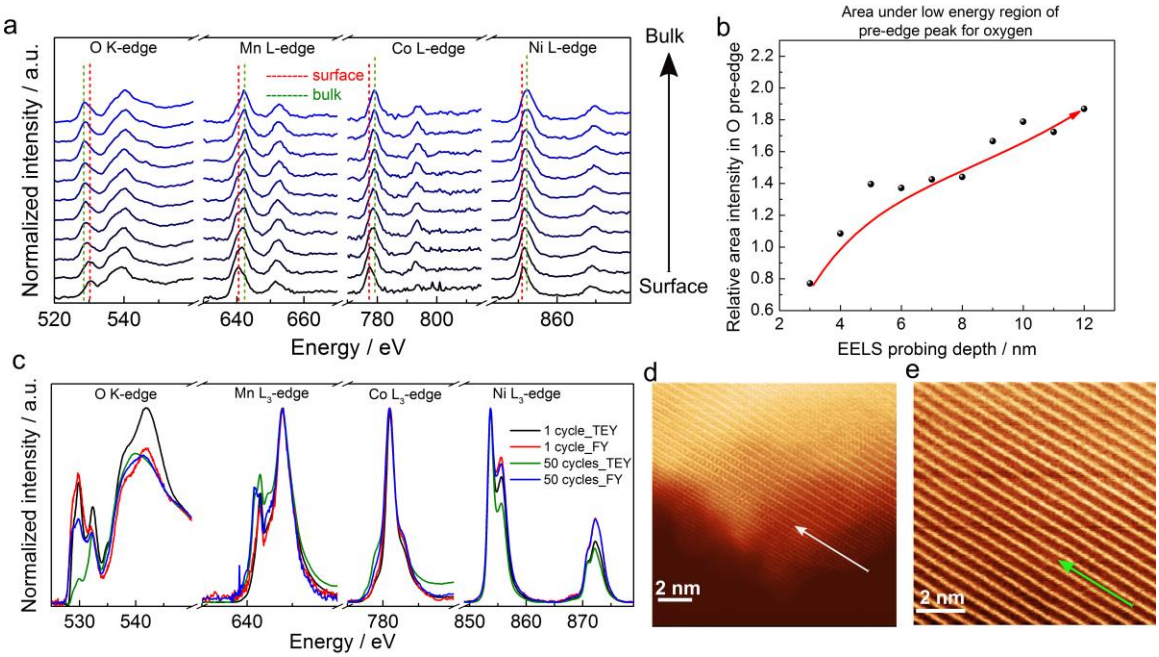
a
O K-edge
Mn L-edge
Co L-edge
Ni L-edge
surface
bulk
Normalized intensity / a.u.
Energy / eV
Bulk
Surface
b
Area under low energy region of pre-edge peak for oxygen
Relative area intensity in O pre-edge
EELS probing depth / nm
c
O K-edge
Mn L3-edge
Co L3-edge
Ni L3-edge
1 cycle_TEY
1 cycle_FY
50 cycles_TEY
50 cycles_FY
Normalized intensity / a.u.
Energy / eV
d
2 nm
e
2 nm

Figure 7.